Chemistry–A European Journal
Research Article
doi.org/10.1002/chem.202500058
Chemistry Europe
European Chemical Societies Publishing
www.chemeurj.org

Understanding the Nitrogen Reduction Reaction Mechanism on $CuFeO_2$ Photocathodes

Julian Beßner[a] and Timo Jacob*[a, b, c]

This study investigates the reaction pathways for the conversion of N_3 to NH_2 on $CuFeO_2$ (CFO) by employing density functional theory (DFT) calculations. Concentrating on the most stable (012) surface orientation, two systems were examined: the pristine (012) surface and the corresponding oxygen defective surface. To find the thermodynamic stable pathway, the associative Heyrovský mechanism was considered, containing four different reaction pathways. The reaction intermediates predominantly interact with the iron sites on the surface, following the distal alternating reaction pathway via the formation of hydrazine. Introducing oxygen defects changes the reaction mechanism to a Mars–van-Krevelen-type mechanism, avoiding the formation of hydrazine, while the Gibbs free energy of the first hydrogenation step is lowered by 1.17 eV (from 2.17 to 1.00 eV). Analyzing the charge density distribution reveals that an oxygen defective surface enables CFO to facilitate a π–backdonation between iron sites and the reaction intermediates, increasing the intermediate–surface interaction. This indicates an enhanced catalytic activity for the nitrogen reduction reaction (NRR) by generating oxygen lattice defects in CFO.

Introduction

The electrochemical conversion of N_2 to NH_2 is one of society's biggest challenges towards a sustainable and energy-saving economy, as ammonia is an indispensable material widely used in producing agricultural fertilizers, and other industrial chemicals.[1–3] The importance of ammonia production is emphasized by the development of the Haber–Bosch-process in the early 20th century, leading to a quadruple growth of the global population.[2] However, industrial ammonia synthesis engulfs about 2% of the world's total energy and yields more than 300 million tons of carbon dioxide emissions.[4,5] Based on these considerations, there is a strong incentive to investigate and develop an eco-friendly, ambient, and sustainable method for N_2 conversion. Several strategies have been introduced toward environmentally friendly ammonia production, including biomimetic, thermocatalytic, plasmacatalytic, photocatalytic, and electrocatalytic approaches.[6,7] Among these, the photoelectrocatalytic NRR presents a unique way of producing ammonia under mild conditions (<300 °C, <1 MPa) by using the inexhaustible solar energy, which could be a solution for smaller-scale and sustainable production sites.[8,9]

Recent studies have shown that earth-abundant transition metal carbides,[10] nitrides,[11] sulfides,[12,13] and oxides[14] exhibit comparable NRR activity to most noble metals. In particular, metal oxides have garnered significant attention for their ease of synthesis, favorable catalytic properties, and high stability. One of the promising materials is copper, as it has already shown high activity for other reduction reactions like the CO_2 reduction reaction (CO_2RR).[15,16] Further, experimental and theoretical studies indicate high activity for copper and copper oxide compounds for the CO_2RR and the reduction of nitrate to ammonia.[17] However, binary copper oxides show degradation processes under reaction conditions, limiting their stability as electrode material.[18–20]

Beyond that, other binary metal oxides, such as iron oxide, have shown similar catalytic NRR performance.[21,22] As Yang *et al.* demonstrate, engineering the surface morphology of iron oxides to generate a vacancy-rich heterostructure can promote the active sites and further the NRR performance.[23] Moreover, not only do the oxides of these two metals, *i.e.* copper and iron, indicate beneficial NRR performance but doping of copper by iron changes the *d*–band center, and facilitates the adsorption of NRR intermediates.[24] By combining the advantages of metals and their oxides, spinel oxide $CuFe_2O_4$ has demonstrated promising catalytic behavior for nitrate reduction and the NRR, particularly when enriched with oxygen vacancies.[17,25] CFO is widely used in photocatalytic reactions such as water splitting or CO_2RR.[26–29] The *p*–type semiconductor has an optimal band edge alignment for visible light absorption and belongs to the delafossite oxides ($CuMO_2$, M = Al, Ga, Fe, Cr, and Mn) with the lowest band gap (1.15–1.5 eV) among these compounds.[30–32] Due to the low efficiency towards the competing HER, CFO has been implemented in photoelectrochemical setups to yield solar fuel from CO_2 for example.[33–35] The additional metal

[a] J. Beßner, Prof. Dr. T. Jacob
Institute of Electrochemistry, Ulm University, Albert-Einstein-Allee 47, 89081 Ulm, Germany
E-mail: timo.jacob@uni-ulm.de
[b] Prof. Dr. T. Jacob
Helmholtz-Institute Ulm (HIU) for Electrochemical Energy Storage, Helmholtzstr. 11, 89081 Ulm, Germany
[c] Prof. Dr. T. Jacob
Karlsruhe Institute of Technology (KIT), P.O. Box 3640, 76021 Karlsruhe, Germany

Supporting information for this article is available on the WWW under https://doi.org/10.1002/chem.202500058

inside the ternary copper-based oxide can enable a different catalytic selectivity, leading to other bond formations and new intermediates. As reported in recent studies, copper atoms are predominantly involved in the charge transfer process in CFO for the CO_2RR.[28] Hence, regarding the NRR the question arises to which extent the copper or iron centers are involved in the bonding of the NRR intermediates?

In this work, we examine the NRR mechanism on the pristine and the oxygen defective (012) surfaces of CFO. Furthermore, we provide structural and electronic insights into the system along different reaction pathways. In particular, we analyze the bonding nature of the first intermediate, in order to fully understand the orbital contribution of the material and the adsorbate. Our study presents a fundamental understanding and lays the scientific grounds for design approaches that promote CFO's performance in multi-electron reduction reactions.

Results and Discussion

Structural and Electronic Properties of Pristine and Oxygen-Defective (012)−CFO

CFO crystallizes in the space group $R\bar{3}m$ with a planar layer of copper cations, connected by a layer of edge-sharing FeO_3 octahedra, where each O^{2-} ion is coordinated by one Cu^{+} and three Fe^{3+} cations. The Cu−O and Fe−O bond lengths are at 1.85 Å and 2.02 Å, respectively.[36] Based on our previous study, we focus on the (012) surface of CFO as this is the thermodynamically stable surface within the stability region of the material.[36] Moreover, we introduced different oxygen defects at the (012) surface indicated as *top* and *low*, as visualized in Figure 1 (b) and (c), respectively.

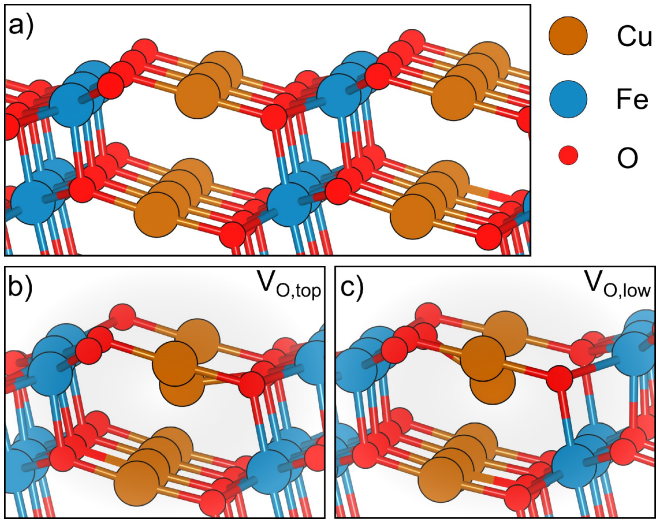

Figure 1. Surface structures of the pristine (012)−CFO (a) surface, the O−defective (top) surface (b), and the O−defective (low) surface (c).

Table 1. Defect formation energy values and change of Bader net charges of oxygen defects.

Defect	ΔE_{def}/eV	Δq_{Cu}/e	Δq_{Fe}/e
$V_{O,top}$	3.18	0.15	0.40
$V_{O,low}$	3.59	0.15	0.41

Table 1 shows the defect formation energy values (ΔE_{def}) and the maximum charge changes at the iron and copper sites due to the oxygen defect. The oxygen vacancy coverage in our work is smaller than 1%. We found similar values for other bulk defects like copper vacancies, doping of magnesium atoms, interstitial oxygen atoms, or other defects.[37,38] Beyond that, oxygen deficiency in $CuFe_2O_4$ and Fe_3O_4 has shown significant improvement regarding the catalytic activity in experimental setups.[17,23]

The oxygen top defect ($V_{O,top}$) is by 0.41 eV more stable than the low defect. The defective surfaces show almost no perturbation due to the missing oxygen atom. Only the copper atom relaxes to a position in the hollow space below the outermost layer. The downward shift for $V_{O,top}$ is about 0.61 Å, while the downward displacement for $V_{O,low}$ lies at 0.71 Å. Moreover, the number of metal−oxygen bonds that must be broken is higher for $V_{O,low}$ than for $V_{O,top}$, yielding a decreased value for ΔE_{def} of $V_{O,top}$. The change of Bader net charge indicates a reduction of the metal atoms. In particular, the iron atoms are responsible for the charge redistribution. In the case of $V_{O,top}$ two superficial iron atoms are reduced to stabilize the charge excess in the surface. For $V_{O,low}$, the excess charge is additionally distributed to the subsurface iron atom below. Beyond that, the absolute magnitude of the iron atoms' magnetic moments changes from 4.20 μ_B to 3.65−3.80 μ_B. Thus, the charge distribution due to the oxygen defect formation results in a selective iron reduction. This negative charge localization within the outermost surface layer can provide an efficient charge transfer to NRR-intermediates. Together with the cavity formed by the downshift of the copper atom the adsorption and hence the activation of the NRR can benefit from this effect.

In the following section, we thoroughly analyze the NRR mechanism on the pristine and defective surface.

Gibbs Free Energy Profiles for the NRR on the Pristine and Oxygen-Defective (012)−CFO

Many studies are investigating the activation of N_2 by modifying the catalyst such that the catalyst develops strong interactions with the N_2 molecule.[39–41] Consequently, the strong interaction of the catalyst with N_2 yields negative Gibbs free energy values for the adsorption of N_2.[23,42,43] In the case of (012)−CFO, we observed a weak end-on N_2 adsorption on the iron atom with a Gibbs free energy of 0.30 eV. The low interaction can be explained by the high coordination of the iron atom which causes the noteworthy stability of CFO's (012) surface.[36] Therefore, its chemical activity is insufficient to activate the N_2 molecule. However, activating N_2 by reactive catalysts is not the only method to facilitate the NRR. Moreover, highly reactive catalysts could experience degradation or

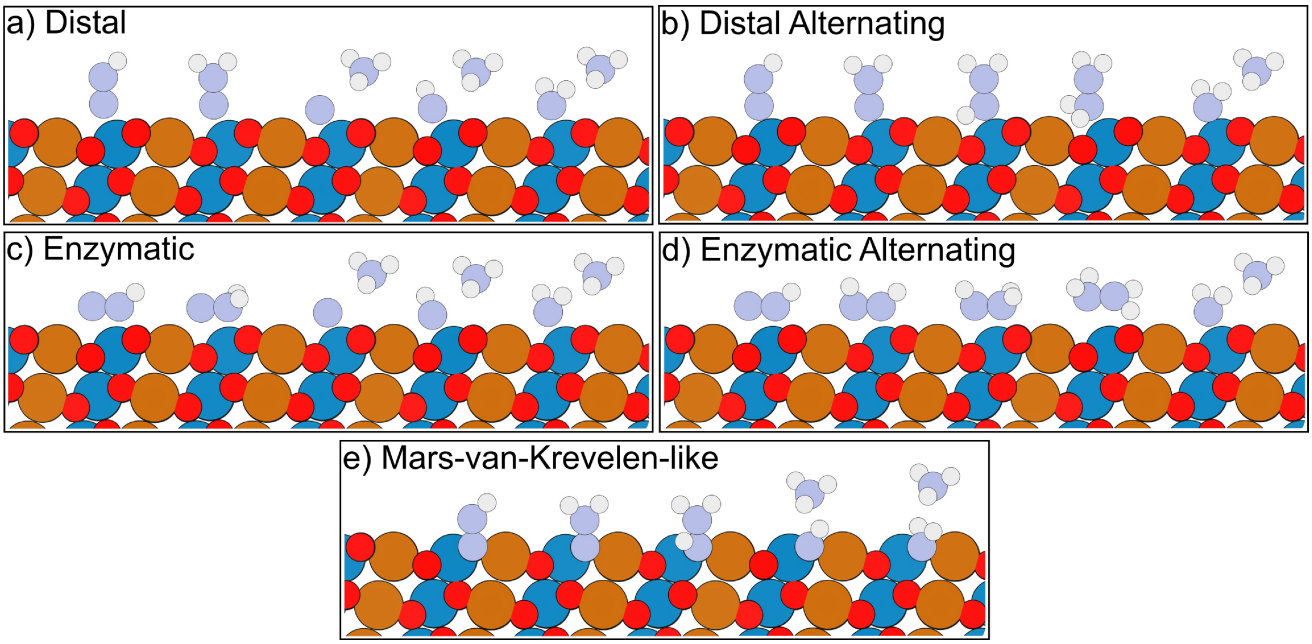

Scheme 1. Schematical representation of the observed reaction pathways of the NRR on CFO.

passivation of the active sites as soon as other compounds approach the active center. One possibility is to perform plasma-enhanced activation of N_2 to improve N_2's interaction with the catalyst.[44–48] Given the ongoing and vibrant debate, along with the variety of views and uncertainties surrounding the activation of N_2, we choose to consider N_2 and NH_3 in the gas phase as reference.

To describe the NRR mechanism, we considered only the reaction following an associative Heyrovský mechanism, as the dissociative pathway requires high energy for the initial N_2 dissociation.[49] The associative mechanism of the NRR can be split into four pathways: distal, distal alternating, enzymatic, and enzymatic alternating pathway (Scheme 1).

Figure 2 summarizes the thermodynamically most stable reaction pathway on the pristine surface. The free energy diagram shows that the first hydrogenation step of N_2 to NNH has the highest energy of 2.17 eV, while the ΔG values for the subsequent steps to two NH_3 molecules are −0.09, −0.38, −0.77, −0.34, and −0.93 eV. Although most theoretical studies suggest the hydrogenation of the outer nitrogen atom, the NNH intermediate on CFO binds via the hydrogenated nitrogen.[50–53] We also tested the other orientation with a slightly higher ΔG of 2.20 eV. Hence, depending on the material and the orientation, the intermediate could also bind via the hydrogenated nitrogen, leading to altering pathways. All following hydrogenation steps are downhill, revealing higher stability for intermediates containing more hydrogens. The thermodynamically favorable mechanism combines the distal and enzymatic altering pathways. Notably, the distal alternating pathway is slightly more stable. The formation of a single nitrogen atom and ammonia is unfavorable as it presents a higher Gibbs free energy value of 3.10 eV compared to the $NHNH_2$ intermediate in the alternating pathways with 1.71 − 1.77 eV as shown in Tables S2 and S3. Thus, the metal atoms on the surface do not offer enough stabilization for the adsorption of N, leading to the formation NO on the surface. In contrast, the intermediates in the alternating pathways, containing more hydrogen atoms, can be stabilized by hydrogen bonding with the oxygen atoms in the outermost surface layer. Thus, the formation of hydrazine (N_2H_4) is preferred, yielding a more negative ΔG value (−0.77 eV) than the previous hydrogenation steps. The Gibbs free energy profile for each associative mechanism is reported in the SI together with the zero-point energy correction and the entropic contribution (Figures S1−S4 and Tables S2−S5).

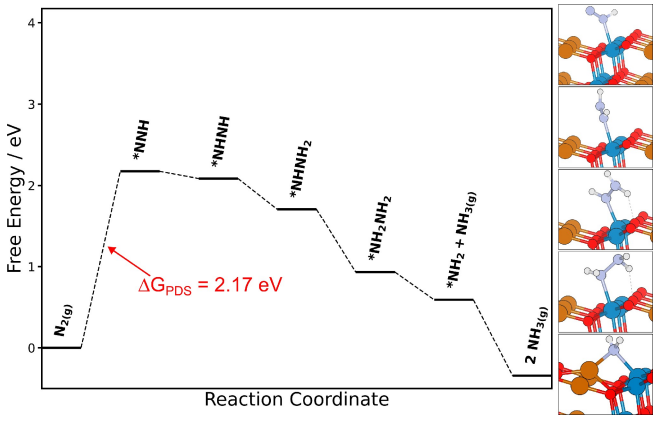

Figure 2. The Gibbs free energy profile of the thermodynamic minimal NRR pathway on the pristine (012)−CFO surface. On top of the diagram are the optimized geometric structures of the thermodynamic reaction pathway.

Furthermore, the intermediates tend to adsorb on the iron site on the pristine surface. The iron sites in the outermost layer are missing one oxygen atom to complete their octahedral

coordination sphere, while the copper atoms are satisfied with two oxygen neighbors. Therefore, the iron site is the preferred active site for most intermediates. In the case of NH_2, the additional bond to the copper atom results in further stabilization of NH_2. Consequently, the copper atom moves from its original position by 0.61 Å, confirming the high flexibility of copper atoms in the surface structure. To calculate the overpotential η we consider $\eta = U_{equilibrium} - U_L$, where $U_L = -2.17$ V and $U_{equilibrium} = -0.17$ V.[54] Thus, the overpotential of the NRR on the pristine (012) surface yields 2.00 V.

Figure 3 shows the NRR Gibbs free energy profiles for the two different oxygen defects. The first hydrogenation process yields a Gibbs free energy change of 1.00 eV for the mechanism on the $V_{O,top}$ surface, while the $V_{O,low}$ (012) surface has a Gibbs free energy change of 1.21 eV. Thus, both oxygen defects possess the same PDS and significantly decrease the Gibbs free energy of the PDS by about 1 eV. Especially, the $V_{O,top}$ structure indicates a larger impact on the stability of the NNH−intermediate since the Gibbs free energy value is less than half of the original value on the pristine (012) surface. Thereby, the defect generation provides a lowered ΔG_{PDS} close to noble metals such as ruthenium.[55]

The following ΔG values of the NRR on the $V_{O,top}$ surface are −0.21, −0.42, −0.95, −0.47, and 0.71 eV. Hence, ΔG for the formation of NH (−0.95 eV) is more negative than the formation of N_2H_4 (−0.77 eV) on the pristine surface. This difference indicates a strong incentive to change the associative reaction pathway to a dissociative pathway.

For the mechanism on the $V_{O,low}$ surface the ΔG values of the NRR are −0.40, −0.64, −0.37, −0.79, and 0.65 eV. Here, ΔG for the formation of NH (−0.37 eV) is less than half as on the $V_{O,top}$ surface. The NH_2 intermediate is the only mononitrogen intermediate strongly bound in the vacancy, creating an endergonic step for the last hydrogenation. The ΔG values differ for each defect because of the distinct coordination environments of the defect sites, leading to a different intermediate during the second hydrogenation step. As shown in Figure 3, the pathway on the $V_{O,top}$ surface begins with a distal orientation of the intermediates as the NNH−intermediate is hydrogenated at the outer nitrogen, forming NNH_2. On the contrary, the pathway

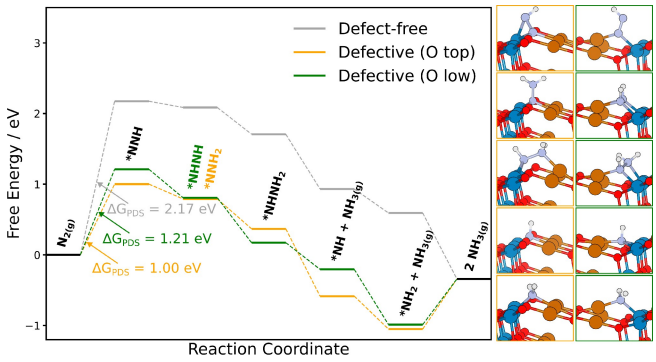

Figure 3. The Gibbs free energy profile of the thermodynamic minimal NRR pathway on the pristine and both O−defective (012)−CFO surfaces. Next to the diagram are the optimized geometric structures of the reaction intermediates on the O (top) defective surface.

on the $V_{O,low}$ surface prefers the enzymatic alternating mechanism, forming a NHNH−intermediate instead of the NNH_2. Hence, the intermediate is orientated horizontally on the defective surface. Although the hydrazine formation is favorable for the mechanism on the pristine surface, both defective surfaces prefer the dissociative step by desorbing NH_3 and forming mononitrogen intermediates. Beyond that, the downward shift of the copper atom in both defects is reversed as the bond formation with the intermediates rearranges the copper atom back to its original position like in the pristine surface (Figure 1a). This results in a reaction mechanism similar to the Mars−van-Krevelen (MvK) pathway, whereas the reactants repair the defective site in the catalyst.[56,57] The MvK mechanism is observed on transition metal nitrides (TMN) where the hydrogenation of the nitrogen atoms in the surface leads to the formation and eventually to the desorption of ammonia.[58] Thus, the oxygen defects enable the MvK mechanism by providing vacancies, which can be filled with adsorbates. Similar trends have been observed in other oxygen vacancy-enriched iron oxides, although the decrease of ΔG_{PDS} was less pronounced.[25,59]

Furthermore, the negative ΔG values of the mononitrogen intermediates lead to the reaction profile not being exergonic for all steps in contrast to the mechanism on the pristine surface. In particular, the last step could be a competing hydrogenation step to the PDS. Moreover, the overpotential of the NRR on the $V_{O,top}$ (012) surface yields 0.83 V, and 1.04 V for the $V_{O,low}$ (012) surface.

Electronic Properties of the (012)−CFO Surface along the NRR

Besides the thermodynamic analysis of the NRR on the pristine and oxygen-defective surface, we investigated the electronic properties of the NRR intermediates, evaluating the projected density of states (pDOS), charge density differences, and Bader net charges. Figure 4 shows the pDOS of the pristine surface, after the first hydrogenation step, and after the last hydrogenation. The corresponding charge density differences are presented on the right-hand side of the figure. As shown in literature and our previous study, the conduction band consists mainly of iron 3*d*−states, while the valence band maximum exhibits copper 3*d*− and oxygen 2*p*−states. The DOS of the surface with NNH adsorbed is very similar to that of the pristine surface. However, there is an additional nitrogen 2*p*−state at 0.7 eV and another at 0.95 eV at the conduction band minimum below the iron 3*d*−states. Transition-metal oxides containing iron exhibit empty 3*d*−orbitals, which can accept the lone pair electrons of N_2, NNH, and further intermediates, leading to an activation of the inert N_2 triple bond.[50] The overlapping of the nitrogen 2*p*−states and the iron 3*d*−states indicates a hybridization, weakening the N–N bonding of the dinitrogen intermediates, which can be seen in the charge accumulation between the iron and the nitrogen atom. Additionally, the N–N bond is elongated to a value of 1.18 Å, and the Bader net charge value of the nitrogen atom bonded to the iron atom is reduced to a value of −0.49 *e*, indicating the acceptance−dona-

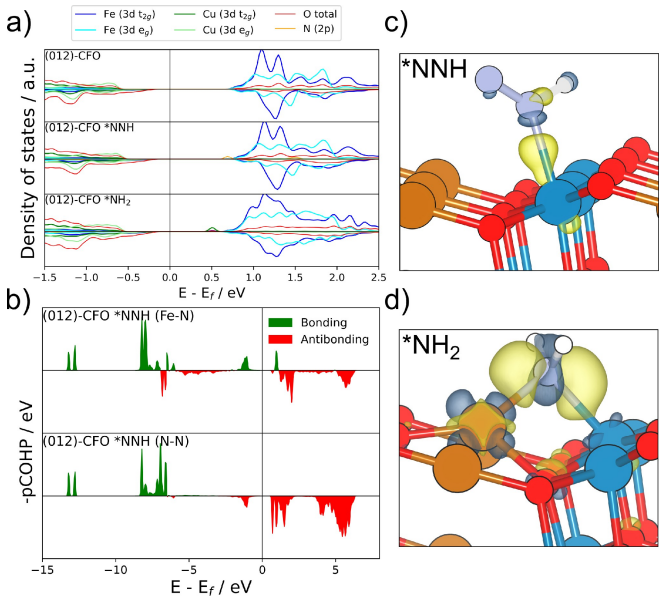

Figure 4. The projected density of states (pDOS) (a) and the projected crystal Hamilton populations (pCOHP) (b) of the pristine (012)−CFO surface of the first intermediate and the charge density difference of NNH (c) and NH_2 (d). The isosurface level was chosen at 0.007 eÅ^{-3}.

tion interaction between the adsorbed NNH-intermediate and the catalytic site. The interaction of the iron−3*d* and nitrogen−2*p* orbitals gives rise to iron being the active site for the first hydrogenation step. The high activity towards the NRR for compounds containing iron has already been reported in literature.[23,39,60] Moreover, contrary to the proposed NRR pathways in literature, where NNH binds via the non-hydrogenated nitrogen atom, we find NNH to adsorb via its N–H group.[23] The pDOS for the other intermediates is reported in Figure S5 in the Supporting Information.

The projected COHP shown in Figure 4 (b) enlightens the bonding nature between the iron being the active site and the nearby nitrogen atom of the adsorbed NNH. Hence, the bonding orbitals are more occupied than the antibonding orbitals, indicating the stabilization of the NNH intermediate with the help of the iron. Notably, the iron−3*d* and nitrogen−2*p* states at 0.95 eV in the pDOS are assigned to the bonding orbitals in the pCOHP in Figure 4 (b), suggesting an improved stability upon electron transfer. Moreover, the interaction between NNH and the iron atom is supported by charge donation from the σ− and π−states of the nitrogen 2*p*−orbitals to the partially-occupied t_{2g} and e_g orbitals of the iron atom. The NH_2 intermediate changes the electronic structure of the system, as it is bound to a copper and an iron atom. Thus, the copper atom is oxidized as the Bader net charge increases from 0.52 *e* to 0.98 *e*. Accordingly, the pDOS shows the formation of an empty 3*d*−e_g state at 0.5 eV and an unoccupied oxygen 2*p*−state. The charge is distributed among the surface atoms to stabilize the catalytic sites on the surface. Consequently, the charge is transferred to the NH_2 intermediate, as the Bader net charge value results in −1.22 *e*. The NH_2 intermediate is the only intermediate interacting with the 3*d*−orbitals of copper. Hence, copper seems to play an inferior role during the NRR mechanism. Depending on the environment, the copper atoms seem to have higher flexibility within the crystal lattice as they can rearrange their position by more than 0.6 Å.

Figure 5 presents the pDOS of the $V_{O,top}$ (012) surface, and with NNH and NH_2 adsorbed. There are two small iron 3*d*−t_{2g}−states at the valence band maximum at −0.5 eV and −0.25 eV, indicating the partial occupation of the iron t_{2g}−orbitals and thus the reduction of the Fe^{3+} to Fe^{2+} due to the oxygen defect. The formation of the oxygen defect causes a shift of the Fermi level towards the conduction band. The adsorption of NNH induces a charge transfer from the Fe^{2+} to the bonded nitrogen atoms in the adsorbate. Thereby, the two iron states in the valence band maximum fade, while 2*p*−states of the nitrogen atoms are occupied and appear in the valence band maximum.

Moreover, the Bader net charge transfer from the iron atoms to the nitrogen atoms amounts to 0.23 *e* and 0.36 *e*. The pCOHP illustrates the decrease of antibonding orbitals and the increase of bonding orbitals between the iron and nitrogen atoms. Hence, the integrated COHP (ICOHP) between the iron and the nitrogen atom of NNH is at −1.68, while the ICOHP value for the interaction on the pristine surface lies at −1.02. Thereby, the iron−nitrogen interaction is enhanced and NNH stabilized. Beyond that, the antibonding character of the nitrogen−nitrogen bond increases on the defective surface (ICOHP: −13.18) compared to the pristine surface (ICOHP: −18.82). Looking at the antibonding orbital contribution in Figure 5 (b), one notices that there is a peak at −0.25 eV in the

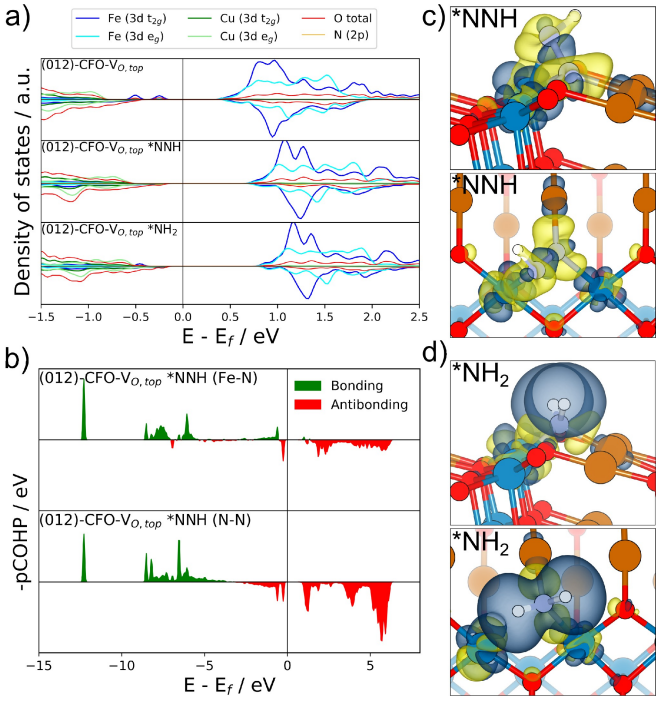

Figure 5. The projected density of states (pDOS) (a) and the projected crystal Hamilton populations (pCOHP) (b) of the oxygen (top) defective (012)−CFO surface of the first intermediate and the charge density difference of NNH (c) and NH_2 (d). The isosurface level was chosen at 0.007 eÅ^{-3}.

nitrogen−nitrogen bond but also in the iron−nitrogen bond, indicating a π−backdonation of the 3d−t_{2g}−iron orbital to the nitrogen's antibonding 2p orbital. Thus, this π−backdonation strengthens the iron−nitrogen bonding and weakens the nitrogen−nitrogen interaction. Consequently, the charge density difference presents a charge depletion between the nitrogen atoms and a large charge accumulation between the inner nitrogen atom and the neighboring copper and iron atoms. Beyond that, the outer nitrogen atom forms a bond with the other iron atom, leading to an elongated N–N bond of 1.31 Å in NNH at the oxygen vacancy. The oxygen (low) defect exhibits a weaker activation of the NNH intermediate as reported in Figure S7.

Hence, the Gibbs free energy is significantly lowered for the first hydrogenation step in the oxygen−defective surface. While NNH oxidizes the two iron atoms close to the oxygen defect, the other dinitrogen intermediates NNH_2 and $NHNH_2$ are bonded only to one of the iron atoms, leaving the other iron atom reduced. Thus, there is an iron 3d−t_{2g} state at −0.25 eV in the valence band maximum as reported in the supporting information (Figure S6). The pDOS of the NNH_2−intermediate indicates a partially occupied 3d−e_g orbital whereas the $NHNH_2$−intermediate exhibits an iron 3d−t_{2g} orbital in the valence band maximum. Accordingly, the NRR intermediates interact primarily with the iron 3d−orbitals on the oxygen−-defective surface, suggesting the acceptance−donation mechanism works via the iron atoms at the surface.

Conclusions

In summary, we studied the NRR activity of $CuFeO_2$ using electronic structure simulations. We explored four different types of mechanisms on the pristine (012) surface of CFO, whereby our study suggests the thermodynamic stable pathway is a combination of the distal alternating and enzymatic alternating pathways via the formation of hydrazine. The first hydrogenation is the most energetically demanding step with a limiting potential of $U_L = -2.17$ V. The Gibbs free energy values of the following hydrogenation steps are all downhill. Beyond that, all intermediates predominantly interact via σ− or π−charge donations with the iron sites at the surface. Introducing oxygen vacancies can significantly decrease the limiting potential U_L to −1.00 V. In particular, the reaction pathway changes to a MvK-type mechanism, avoiding the formation of hydrazine on oxygen-defective surfaces. Mononitrogen intermediates impact the oxygen vacancy by repairing the defective surface to its pristine structure. Hence, oxygen lattice defects change the reaction pathway notably.

The high activity of the oxygen defective surface results from the localized iron 3d−t_{2g} states near the Fermi level induced by the oxygen vacancy. As shown in the pDOS and pCOHP analysis, the iron atoms in the oxygen defective surface enable the π−backdonation. Therefore, oxygen vacancies enhance the activation of dinitrogen intermediates. Consequently, the iron atoms in $CuFeO_2$ contribute predominantly to the bonding of NRR intermediates.

This work developed a detailed description of the thermodynamic activity of this ternary copper−based oxide. Moreover, we shed light on the nature of the active sites and the structural and electronic influence of oxygen defects on the NRR. However, further experimental and theoretical studies are necessary to obtain realistic assessments regarding defect stabilities and other effects on the reaction, such as solvation properties. Thus, our results may encourage further experimental and theoretical efforts to explore other ternary copper- or iron-based oxides and their potential applications and provides insights for defect engineering.

Computational Details

All calculations were performed using the Vienna Ab Initio Simulation Package (VASP) version 6.2 to facilitate DFT-based spin-polarized simulations with the projector augmented wave (PAW) approach.[62–64] The Perdew-Burke-Ernzerhof (PBE) exchange−correlation functional was used in connection with Hubbard's U−correction (PBE + U) in order to improve the description of the electronic structure of the oxide systems.[65] To handle the Coulomb interaction of the d electrons of the material the DFT + U method with the rotationally invariant formulation of Dudarev was introduced to the d electrons of Cu (U = 8 eV) and Fe (U = 4 eV).[66] The U values have been optimized in our previous study and agree with published U values for mixed transition metal oxides in literature.[33,36]

The Brillouin Zone (BZ) of the surface unit cell was sampled with a $4 \times 2 \times 1$ Monkhorst-Pack k−point grid. For the density of states results, we chose a denser k−point grid ($8 \times 4 \times 1$). Calculations were considered to be converged when the Hellmann−Feynman forces and self-consistent total electronic energy convergence thresholds reached 0.02 eV Å^{-1} and 10^{-5} eV, respectively. For the basis sets, the plane wave cut-off was set to 500 eV. The surface slabs were replicated with a 10 Å vacuum region added in the direction perpendicular to the surface to avoid artificial interactions between periodic replicas. The surface was modeled with a (3×1) three-layer supercell, containing 108 atoms. Only the upper two layers and the adsorbed species were fully relaxed, while the bottom layer was fixed to the bulk-truncated structure. Side views of the geometries have been created with Vesta.[67]

Supporting Information

The authors have cited additional references within the Supporting Information.[61]

Acknowledgements

The authors acknowledge support by the state of Baden-Württemberg through bwHPC and the German Research Foundation (DFG) through grant no INST 40/575-1 FUGG (JUSTUS 2 cluster). Additional simulations were performed on the high-performance computing cluster ULMIX provided by the Institute of Electrochemistry at Ulm University. Furthermore, support by the DFG through the collaborative research center SFB-1316 (project 327886311), the priority program SPP−2370 (project 502202153), and project 501805371 is gratefully

acknowledged. Open Access funding enabled and organized by Projekt DEAL.

Conflict of Interests

The authors declare no conflict of interest.

Data Availability Statement

The data that support the findings of this study are openly available in Zenodo at https://doi.org/10.5281/zenodo.14260569, reference number 14260569.

Keywords: Computational Chemistry · $CuFeO_2$ · Nitrogen Reduction Reaction · Oxygen Vacancy Engineering · Photocatalysis

[1] J. G. Chen, R. M. Crooks, L. C. Seefeldt, K. L. Bren, R. M. Bullock, M. Y. Darensbourg, P. L. Holland, B. Hoffman, M. J. Janik, A. K. Jones, M. G. Kanatzidis, P. King, K. M. Lancaster, S. V. Lymar, P. Pfromm, W. F. Schneider, R. R. Schrock, *Science* **2018**, *360*, eaar6611.
[2] A. J. Medford, M. C. Hatzell, *ACS Catal.* **2017**, *7*, 2624.
[3] S. L. Foster, S. I. P. Bakovic, R. D. Duda, S. Maheshwari, R. D. Milton, S. D. Minteer, M. J. Janik, J. N. Renner, L. F. Greenlee, *Nat. Catal.* **2018**, *1*, 490.
[4] R. B. Jackson, J. G. Canadell, C. Le Quéré, R. M. Andrew, J. I. Korsbakken, G. P. Peters, N. Nakicenovic, *Nat. Clim. Change* **2016**, *6*, 7.
[5] A. J. Martín, T. Shinagawa, J. Pérez-Ramírez, *Chem* **2019**, *5*, 263.
[6] Q. Wang, J. Guo, P. Chen, *J. Energy Chem.* **2019**, *36*, 25, special Issue: In celebration of the 70th anniversary of Dalian Institute of Chemical Physics, Chinese Academy of Sciences.
[7] R. Shi, X. Zhang, G. I. N. Waterhouse, Y. Zhao, T. Zhang, *Adv. Energy Mater.* **2020**, *10*, 2000659.
[8] S. Wang, F. Ichihara, H. Pang, H. Chen, J. Ye, *Adv. Funct. Mater.* **2018**, *28*, 1803309.
[9] D. Zhu, L. Zhang, R. E. Ruther, R. J. Hamers, *Nat. Mater.* **2013**, *12*, 836.
[10] X. Ren, J. Zhao, Q. Wei, Y. Ma, H. Guo, Q. Liu, Y. Wang, G. Cui, A. M. Asiri, B. Li, B. Tang, X. Sun, *ACS Cent. Sci.* **2019**, *5*, 116.
[11] R. Zhang, Y. Zhang, X. Ren, G. Cui, A. M. Asiri, B. Zheng, X. Sun, *ACS Sustainable Chem. Eng.* **2018**, *6*, 9545.
[12] X. Li, T. Li, Y. Ma, Q. Wei, W. Qiu, H. Guo, X. Shi, P. Zhang, A. M. Asiri, L. Chen, B. Tang, X. Sun, *Adv. Energy Mater.* **2018**, *8*, 1801357.
[13] L. Zhang, X. Ji, X. Ren, Y. Ma, X. Shi, Z. Tian, A. M. Asiri, L. Chen, B. Tang, X. Sun, *Adv. Mater.* **2018**, *30*, 1800191.
[14] Y. Liu, H. Bai, Q. Zhang, Y. Bai, X. Pang, F. Wang, Y. Yang, J. Ding, W. Fan, W. Shi, *Chem. Eng. J.* **2021**, *413*, 127453.
[15] M. Behrens, F. Studt, I. Kasatkin, S. Kühl, M. Hävecker, F. Abild-Pedersen, S. Zander, F. Girgsdies, P. Kurr, B.-L. Kniep, M. Tovar, R. W. Fischer, J. K. Nørskov, R. Schlögl, *Science* **2012**, *336*, 893.
[16] J. Graciani, K. Mudiyanselage, F. Xu, A. E. Baber, J. Evans, S. D. Senanayake, D. J. Stacchiola, P. Liu, J. Hrbek, J. F. Sanz, J. A. Rodriguez, *Science* **2014**, *345*, 546.
[17] H. Zhu, S. Dong, X. Du, H. Du, J. Xia, Q. Liu, Y. Luo, H. Guo, T. Li, *Catal. Sci. Technol.* **2022**, *12*, 4998.
[18] H. Xing, L. E, Z. Guo, D. Zhao, X. Li, Z. Liu, *Inorg. Chem. Front.* **2019**, *6*, 2488.
[19] Y. J. Jang, A. E. Lindberg, M. A. Lumley, K.-S. Choi, *ACS Energy Lett.* **2020**, *5*, 1834.
[20] Q. Wang, Y. Zhang, Y. Liu, K. Wang, W. Qiu, L. Chen, W. Li, J. Li, *J. Electroanal. Chem.* **2022**, *912*, 116252.
[21] Q. Liu, X. Zhang, B. Zhang, Y. Luo, G. Cui, F. Xie, X. Sun, *Nanoscale* **2018**, *10*, 14386.
[22] C. H. Lee, S. Pahari, N. Sitapure, M. A. Barteau, J. S.-I. Kwon, *ACS Catal.* **2023**, *13*, 8336.
[23] X. Yang, Y. Tian, S. Mukherjee, K. Li, X. Chen, J. Lv, S. Liang, L.-K. Yan, G. Wu, H.-Y. Zang, *Angew. Chem. Int. Ed.* **2023**, *62*, e202304797.
[24] Y. Kong, C. Lv, G. Chen, *Mater. Today Energy* **2023**, *31*, 101215.
[25] A. Y. Bhat, A. U. Bashir, P. Jain, M. A. Bhat, P. P. Ingole, *Small* **2024**, *20*, 2403319.
[26] A. Wuttig, J. W. Krizan, J. Gu, J. J. Frick, R. J. Cava, A. B. Bocarsly, *J. Mater. Chem. A* **2017**, *5*, 165.
[27] U. Kang, S. K. Choi, D. J. Ham, S. M. Ji, W. Choi, D. S. Han, A. Abdel-Wahab, H. Park, *Energy Environ. Sci.* **2015**, *8*, 2638.
[28] S. H. Yoon, U. Kang, H. Park, A. Abdel-Wahab, D. S. Han, *Catal. Today* **2019**, *335*, 345, advances in photo(electro)catalysis for environmental applications and chemical synthesis.
[29] H. Xu, R. Wu, J.-Y. Zhang, W. Han, L. Chen, X. Liang, C. Y. Haw, P. Mazzolini, O. Bierwagen, D.-C. Qi, K. H. L. Zhang, *ACS Appl. Electr. Mater.* **2021**, *3*, 1834.
[30] H. Kawazoe, M. Yasukawa, H. Hyodo, M. Kurita, H. Yanagi, H. Hosono, *Nature* **1997**, *389*, 939.
[31] M. A. Marquardt, N. A. Ashmore, D. P. Cann, *Thin Solid Films* **2006**, *496*, 146, proceedings of the Fourth International Symposium on Transparent Oxide Thin Films for Electronics and Optics (TOEO-4).
[32] M. S. Prévot, N. Guijarro, K. Sivula, *ChemSusChem* **2015**, *8*, 1359.
[33] C. Baiano, E. Schiavo, C. Gerbaldi, F. Bella, G. Meligrana, G. Talarico, P. Maddalena, M. Pavone, A. B. Muñoz-Garca, *J. Mol. Catal.* **2020**, *496*, 111181.
[34] X. Yang, E. A. Fugate, Y. Mueanngern, L. R. Baker, *ACS Catal.* **2017**, *7*, 177.
[35] J. Gu, A. Wuttig, J. W. Krizan, Y. Hu, Z. M. Detweiler, R. J. Cava, A. B. Bocarsly, *J. Phys. Chem. C* **2013**, *117*, 12415.
[36] J. Beßner, S. E. Bogenrieder, R. Neuhoff, B. Kirchhoff, T. Jacob, *J. Phys. Chem. C* **2024**, *128*, 10146.
[37] M. Ferri, J. Elliott, M. Farnesi Camellone, S. Fabris, S. Piccinin, *J. Phys. Chem. C* **2019**, *123*, 29589.
[38] E. Schiavo, C. Latouche, V. Barone, O. Crescenzi, A. B. Muñoz-García, M. Pavone, *Phys. Chem. Chem. Phys.* **2018**, *20*, 14082.
[39] D. Ma, Z. Zeng, L. Liu, X. Huang, Y. Jia, *J. Phys. Chem. C* **2019**, *123*, 19066.
[40] X. Liu, J. Xiao, S. Ma, C. Shi, L. Pan, J.-J. Zou, *ChemNanoMat* **2021**, *7*, 684.
[41] Y. Qian, Y. Liu, Y. Zhao, X. Zhang, G. Yu, *EcoMat* **2020**, *2*, e12014.
[42] C. H. Lee, S. Pahari, N. Sitapure, M. A. Barteau, J. S.-I. Kwon, *ACS Catal.* **2023**, *13*, 8336.
[43] Z. Bai, Y. Liu, W. Zhang, *J. Phys. Chem. Solids* **2024**, *184*, 111664.
[44] P. Peng, C. Schiappacasse, N. Zhou, M. Addy, Y. Cheng, Y. Zhang, K. Ding, Y. Wang, P. Chen, R. Ruan, *ChemSusChem* **2019**, *12*, 3702.
[45] L. R. Winter, J. G. Chen, *Joule* **2021**, *5*, 300.
[46] J. Hong, S. Prawer, A. B. Murphy, *ACS Sustainable Chem. Eng.* **2018**, *6*, 15.
[47] P. Mehta, P. Barboun, F. A. Herrera, J. Kim, P. Rumbach, D. B. Go, J. C. Hicks, W. F. Schneider, *Nat. Catal.* **2018**, *1*, 269.
[48] K. H. R. Rouwenhorst, H.-H. Kim, L. Lefferts, *ACS Sustainable Chem. Eng.* **2019**, *7*, 17515.
[49] S. Wang, C. Qian, S. Zhou, *Mater. Chem. Front.* **2023**, *7*, 4259.
[50] S. Liu, Y. Liu, Z. Cheng, Y. Tan, Y. Ren, T. Yuan, Z. Shen, *ACS Appl. Mater. Interfaces* **2021**, *13*, 40590.
[51] D. Ma, Z. Zeng, L. Liu, X. Huang, Y. Jia, *J. Phys. Chem. C* **2019**, *123*, 19066.
[52] Y. Tian, B. Chang, G. Wang, L. Li, L. Gong, B. Wang, R. Yuan, W. Zhou, *J. Mater. Chem. A* **2022**, *10*, 2800.
[53] S. Wang, C. Qian, S. Zhou, *Mater. Chem. Front.* **2023**, *7*, 4259.
[54] O. Westhead, R. Tort, M. Spry, J. Rietbrock, R. Jervis, A. Grimaud, A. Bagger, I. E. Stephens, *Faraday Discuss.* **2023**, *243*, 321.
[55] E. Skúlason, T. Bligaard, S. Gudmundsdóttir, F. Studt, J. Rossmeisl, F. Abild-Pedersen, T. Vegge, H. Jónsson, J. K. Nørskov, *Phys. Chem. Chem. Phys.* **2012**, *14*, 1235.
[56] S. Y. Park, Y. J. Jang, D. H. Youn, *Catalysts* **2023**, *13*.
[57] S. Qiang, F. Wu, J. Yu, Y.-T. Liu, B. Ding, *Angew. Chem. Int. Ed.* **2023**, *62*, e202217265.
[58] Y. Abghoui, E. Skúlason, *Catal. Today* **2017**, *286*, 69, nitrogen Activation.
[59] T. Takashima, T. Mochida, H. Irie, *Sustain. Energy Fuels* **2023**, *7*, 2740.
[60] X.-F. Li, Q.-K. Li, J. Cheng, L. Liu, Q. Yan, Y. Wu, X.-H. Zhang, Z.-Y. Wang, Q. Qiu, Y. Luo, *J. Am. Chem. Soc.* **2016**, *138*, 8706.
[61] a) J. K. Nørskov, J. Rossmeisl, A. Logadottir, L. Lindqvist, J. R. Kitchin, T. Bligaard, H. Jónsson, *The J. of Phys. Chem. B* **2004**, *108*, 17886; b) Thomas C. Allison, *NIST-JANAF Thermochemical Tables* – SRD 13 **2013**; c) K. L. Svane, M. Reda, T. Vegge, H. A. Hansen, *ChemSusChem* **2019**, *12*, 5133; d) V. Wang, N. Xu, J.-C. Liu, G. Tang, W.-T. Geng, *Comp. Phys. Commun.* **2021**, *267*, 108033; e) R. F. W. Bader, *Acc. of Chem. Res.* **1985**, *18*, 9–15; f) V. L. Deringer, A. L. Tchougréeff, R. Dronskowski, *The J. of Phys. Chem. A* **2011**, *115*, 5461; g) S. Maintz, V. L. Deringer, A. L. Tchougréeff, R. Dronskowski, *J. of Comp. Chem.* **2016**, *37*, 1030; h) S. Grimme, *J. of Comp. Chem.* **2006**, *27*, 1787; i) S. Grimme, S. Ehrlich, L. Goerigk, *J. of*

Comp. Chem. **2011**, *32*, 1456; j) K. Bhola, J. J. Varghese, L. Dapeng, Y. Liu, S. H. Mushrif, *J. Phys. Chem. C* **2017**, *121*, 21343.
[62] G. Kresse, D. Joubert, *Phys. Rev. B* **1999**, *59*, 1758.
[63] G. Kresse, J. Furthmüller, *Phys. Rev. B* **1996**, *54*, 11169.
[64] W. Kohn, L. J. Sham, *Phys. Rev.* **1965**, *140*, A1133.
[65] J. P. Perdew, K. Burke, M. Ernzerhof, *Phys. Rev. Lett.* **1996**, *77*, 3865.
[66] S. L. Dudarev, G. A. Botton, S. Y. Savrasov, C. J. Humphreys, A. P. Sutton, *Phys. Rev. B* **1998**, *57*, 1505.
[67] K. Momma, F. Izumi, *J. Appl. Crystallogr.* **2011**, *44*, 1272.

Manuscript received: January 22, 2025
Accepted manuscript online: February 7, 2025
Version of record online: ■■, ■■

RESEARCH ARTICLE

We provide a detailed analysis of the nitrogen reduction mechanism on the pristine and oxygen defective (012) surface of $CuFeO_2$. DFT + *U* calculations examine the stability of reaction intermediates and provide mechanistic insights. Beyond that, we shed light on the active sites' orbital contributions and the oxygen defects' electronic impact.

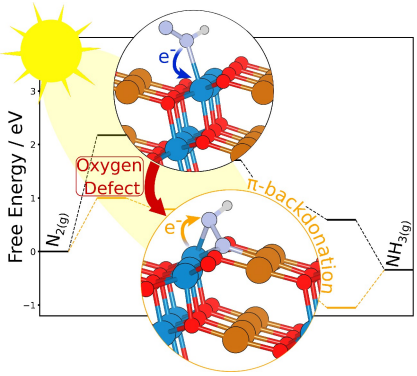

*J. Beßner, Prof. Dr. T. Jacob**

1 – 9

Understanding the Nitrogen Reduction Reaction Mechanism on $CuFeO_2$ Photocathodes